# Accepted Manuscript

A comparative study of structural and electrical properties in lead-free BCZT ceramics: influence of the synthesis method

Indrani Coondoo, Neeraj Panwar, Denis Alikin, Igor Bdikin, Saikh S. Islam, Anton Turygin, Vladimir Ya Shur, Andrei L. Kholkin

Please cite this article as: I. Coondoo, N. Panwar, D. Alikin, I. Bdikin, S.S. Islam, A. Turygin, V.Y. Shur, A.L. Kholkin, A comparative study of structural and electrical properties in lead-free BCZT ceramics: influence of the synthesis method, *Acta Materialia* (2018), doi: 10.1016/j.actamat.2018.05.029.

# A comparative study of structural and electrical properties in lead-free BCZT ceramics: influence of the synthesis method

Indrani Coondoo[1,*], Neeraj Panwar[2], Denis Alikin[1,3], Igor Bdikin[4], Saikh S. Islam[5], Anton Turygin[3], Vladimir Ya. Shur[3] and Andrei L. Kholkin[1,3]

[1]*Department of Physics & CICECO – Aveiro Institute of Materials, University of Aveiro, 3810-193 Aveiro, Portugal*

[2]*Department of Physics, Central University of Rajasthan, Bandarsindri-305817, Rajasthan, India*

[3]*School of Natural Sciences and Mathematics, Ural Federal University, 620026 Ekaterinburg, Russia*

[4]*TEMA-NRD, Mechanical Engineering Department, Aveiro Institute of Nanotechnology, University of Aveiro, 3810-193 Aveiro, Portugal*

[5]*Centre for Nanoscience and Nanotechnology, Jamia Millia Islamia (Central University) New Delhi, India*

## Abstract

In the present work, various grain size phenomena were studied in promising lead-free piezoelectric ceramics $(Ba_{0.85}Ca_{0.15})(Zr_{0.10}Ti_{0.90})O_3$ fabricated via chemical and conventional oxide methods. Phase composition was ascertained by the Rietveld refinement. Average grain size estimated from the microstructure was ~1.5 $\mu$m in the sol-gel derived ceramic (SG-BCZT) which was much smaller than that obtained in coarse grained (~27 $\mu$m) sample prepared by solid state method (SS-BCZT). Systematic investigation of various functional properties *viz.* dielectric, ferroelectric, piezoelectric and impedance emphasized the profound influence of grain size effects. The increase in grain boundary volume fraction enhanced diffuseness while lowered the dielectric peak in SG-BCZT. Similarly, increase in elastic stiffness and progressive hindrance to domain wall movements, resulted in a decrease of the remnant polarization and the associated piezoelectric charge coefficient values in small-grained SG-BCZT sample. Accordingly, higher Young's modulus value of 158.3 GPa was observed in SG-BCZT as compared to 117.9 GPa in SS-BCZT. Local-area piezoresponse force microscopy (PFM) images revealed lamellar domains with periodicity 250±90 nm in SS-BCZT while small sized fractal-like irregular domains with an estimated domain width of 150±60 nm were registered in SG-BCZT. Complex impedance spectroscopy results along with grain boundary conductivity were also guided by grain size effect. The mechanisms of grain size driven effects and their impact on the functional properties were discussed.

**\* Corresponding author´s email: indrani.coondoo@ua.pt;  indrani.coondoo@gmail.com**

## 1. Introduction

Barium titanate (BTO) is an archetypical electroceramic widely used in the capacitor industry for its exceptional properties *viz.* very high dielectric constant, low dielectric loss and low temperature coefficient of the dielectric constant [1]. It exhibits four polymorphs and three transitions (i) rhombohedral (*R*) →orthorhombic (*O*), (ii) *O*→tetragonal (*T*) which are *ferro-ferro*electric phase transitions and (iii) *T*→cubic (*C*) that represents the ferroelectric to paraelectric transformation. With regard to the piezoelectric properties, it has an electromechanical coupling factor, $k_{33}$ ~0.50 and piezoelectric charge coefficient, $d_{33}$ ~190 pC/N [2]. Nevertheless, its performance as a piezoelectric material is subpar, when compared with PZT, thereby limiting its wider applications as actuators and sensors. To enhance the piezoelectric properties, several BaTiO$_3$-based solid solutions with different *A*- and *B*-site substituents (where typically, *A*=Ca, Sr, La; *B*=Nb, Ta, Zr) have been studied. Of particular interest is the MPB composition (Ba$_{0.85}$Ca$_{0.15}$)(Zr$_{0.10}$Ti$_{0.90}$)O$_3$ [hereinafter called BCZT], that has garnered a huge attention owing to its exceptionally high piezoelectric coefficient ($d_{33}$ = 620 pC/N) [3]. A majority of work carried out in relation with the influence of dopants/substituents in BCZT-based materials was done on conventionally synthesized ceramics using the solid state reaction route, involving high calcination (1300 °C, 3h) and sintering temperatures (≥1450 °C, 3h) [4-9]. Such fabrication process apparently results in a coarse grained (grain size >10 $\mu$m) microstructure, which is mechanically unstable and imposes a limitation towards realization of device miniaturization. Alternatively, the wet-chemical processes or solution routes are utilized that allow lowering the crystallization temperature along with additional potential advantages like better compositional homogeneity, chemical purity, controlled stoichiometry, better sinterability and a microstructure with sub-10 $\mu$m grain size. However, control of the complex chemical reactions involved in these chemical routes is experimentally challenging because all the reactants must be in a homogeneous liquid phase during the synthesis reaction. In particular

2

for multi-component compounds such as BCZT that involves several precursors, this is highly demanding. Nonetheless, synthesis of BCZT using various wet chemical synthesis techniques including Pechini polymeric precursor method and hydrothermal process have been tried in the past [10-16]. However, neither comparison, nor deep investigation into the grain size effect in both types of ceramics have been undertaken so far.

In a nutshell, all the various synthesis techniques utilizing different preparation conditions affect the final grain (and domain) size that strongly correlates with the physical and/ or electrical properties in a polycrystalline system [17]. The macroscopic functional properties, essentially the dielectric, ferroelectric and piezoelectric properties are dependent on both *intrinsic* and *extrinsic* contributions, which are expected to be influenced by grain size [18]. *Intrinsic* contributions arise from the relative ion/cation shift that preserves the ferroelectric crystal structure while *extrinsic* contributions are a consequence of the existence of domain walls and defect dipoles [18,19].

With an objective to unfold the grain-size effect, the present work provides a detailed study on structural and electrical properties through a comparative analysis performed on the dense $(Ba_{0.85}Ca_{0.15})(Zr_{0.10}Ti_{0.90})O_3$ ceramics synthesised by the sol-gel and conventional solid state reaction method. Moreover, it is noteworthy that size effect studies on bulk ceramic is apparently more convenient in comparison to thin films. In case of ferroelectric thin films with thickness of the order of $\leq 1\mu$m, the interface between film and electrode is of major concern because the influence of the depolarization field associated with the screening charges in the electrodes, lying in close proximity to the interface with the dielectric layer, leads to thickness-dependent rather than grain size driven electrical properties [20]. On the other hand, owing to the much larger thickness of bulk ceramics ($\sim 10^3$ $\mu$m or more), the influence of the depolarization field is negligible. Also, the size effect in films that are clamped to a substrate may vary from that when removed from it, owing to the lattice and

3

thermal expansion mismatch between the film and the substrate imposing appreciable in-plane stress on the film [20].

It may not be out of place to mention that a few previous reports on comparative studies are available in literature [14,15], which explore relationships between the sintering conditions and only piezoelectric properties of these materials. Present work, on the other hand, provides a comprehensive study correlating the effect of grain size on various other electrical properties as well. An in-depth analysis of X-Ray Diffraction (XRD), along with systematic investigation of the size effect on tetragonal distortion, phase transitions, dielectric, ferroelectric, piezoelectric, impedance and conductivity properties of BCZT ceramics is presented. Moreover, local-area piezoresponse and nanoindentation experiments were additionally explored that provided information on domain configurations and mechanical properties, respectively.

## 2. Experimental details

$Ba_{0.85}Ca_{0.15}Ti_{0.9}Zr_{0.1}O_3$ bulk ceramics were synthesized by two different techniques: solid solution (solid state reaction method; hereafter to be referred as SS-BCZT) and chemical solution (sol-gel process; hereafter to be referred as SG-BCZT) methods. The bulk ceramic obtained by solid state method was prepared by mixing stoichiometric ratios of $BaCO_3$ (99.9%), $CaCO_3$ (99%), $TiO_2$ (99%), and $ZrO_2$ (99%). Heat treatment included calcination at 1200 °C for 6 h, followed by sintering at 1450 °C for 2 h in air. Synthesis of powders by sol-gel synthesis route based on the complexation of alkoxides by acetic acid was accomplished using analytical grade chemicals. Barium acetate ($[Ba(CH_3COO)_2]$, ACS reagent, 99%, Sigma Aldrich), zirconium (IV) propoxide ($[Zr(O(CH_2)_2CH_3)_4]$, 70% solution in propanol, Sigma Aldrich), calcium acetate monohydrate ($[Ca(CH_3COO)_2 \cdot H_2O)]$, 99%, Sigma Aldrich) and titanium isopropoxide ($[(C_{12}H_{28}O_4Ti)]$, ≥ 97%, Sigma Aldrich) were used as precursors. Glacial acetic acid and 2-methoxyethanol were used as the chelating agent and solvent, respectively. For the precursor synthesis, Ba-Ca, and Ti-Zr solutions were prepared

4

separately. Initially 0.5 M barium acetate and calcium acetate was stirred in acetic acid (mole ratio acetate : acetic acid was 1:15) for 1 hour. Separately, 0.5 M titanate solution was prepared by dissolving titanium isopropoxide in 2-methoxyethanol and stirred for 30 minutes at 60 °C to which stoichiometric amount of zirconium-propoxide was added and stirred for 30 minutes. The mole ratio propoxide : 2-methoxyethanol was 1:12. To stabilize this Zr-Ti alkoxide solution, acetylacetone was added (molar ratio acetylacetone : propoxide was 3:1) and stirred for another 1 hour. Subsequently, the Ba-Ca solution was added to the Zr-Ti-solution and stirred at 60 °C and the precursor solution so obtained was thereafter heated at 110 °C, which resulted in the formation of a gel. The whole process of the preparation of the precursor solution was performed in an ambient atmosphere. Finally, the resultant gel was dried overnight at 150 °C and the solidified lumps were ground to fine powders. The synthesis procedure is briefly depicted in Fig. 1.
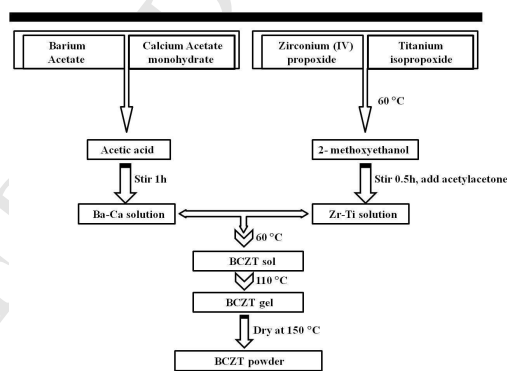


**Figure 1** Flow chart of the preparation process for BCZT powder by sol-gel process.

The obtained powder was calcined at 900 °C for 2h and analysed by X-ray diffraction to confirm the phase formation. Cylindrical pellets were made by uniaxially pressing the calcined powder and subjected to sintering temperature of 1300 °C for a dwelling time of 3h. Phase formation was established by a X-ray diffractometer (Phillips X´Pert diffractometer,

Almelo, Netherlands), using CuK$_\alpha$ radiation in the range 20°≤ 2$\theta$ ≤80° at room temperature. Crystallographic information including phase composition, crystal structure and lattice parameters were comprehended by Rietveld analysis of the X-ray diffraction data using GSAS-EXPGUI refinement software package. The microstructural analysis of the sample was performed on as-sintered surface using a Hitachi S-4100 Field Emission Scanning Electron Microscope equipped with energy- dispersive X-ray spectroscopy (FESEM/EDX). The average grain size was estimated by analysing the area statistics for a selected sub-region of the SEM image, performed by means of the microscope software ImageJ [21]. Further statistical calculations was performed by taking into account the acquired area data to estimate equivalent diameter and obtain the grain size distribution (done using OriginPro 8.5 software). The distribution was fitted using Gaussian function to obtain average grain size. Elemental distribution mapping was done by energy- dispersive X-ray spectroscopy (EDX). Relative density of the sintered ceramic pellets was calculated as the ratio between the apparent density measured by Archimedes´ principle and the crystallographic (theoretical) density. For the various electrical measurements, the sintered samples were polished and silver paste (AGG302, Agar Scientific Ltd., UK) was coated on the larger faces of the disc and cured at 550 °C for 30 min to make electrical contacts. Dielectric and impedance properties were measured as a function of temperature and frequency using a hp4284A precision LCR meter (Agilent, Palo Alto, CA). Ferroelectric hysteresis loops were obtained by current integration. Low-frequency (1 Hz), high-voltage sine waves were applied by the combination of a function generator (HP3325B, Hewlett-Packard Inc., Palo Alto, CA) and a high-voltage amplifier (Trek Model 10/40A, Medina, NY), while charge was measured with a charge to voltage converter. For piezoelectric measurements, the samples were poled in an oil bath with a dc electric field of 3-4 kV/mm at room temperature. The $d_{33}$ piezoelectric coefficient was measured with a Berlincourt piezometer (Channel Products Inc. Chesterland, OH). Domain structure of the ceramic samples were observed by Piezoresponse Force

Microscopy (PFM) technique, performed using scanning probe microscope MFP-3D (Asylum Research, Oxford Instruments, UK). NSG01 commercial Pt/Ir coated tips with curvature radius ~30 nm, spring constant ~1-3 N/m were used. The PFM signal was acquired at 1 V amplitude in Dual AC Resonance Tracking (DART) mode that achieves greater improvement in sensititvity by tracking and operating at the tip-sample contact resonance frequency (≈70-90 kHz). Prior to PFM measurements, the samples were rigorously polished followed by annealing at 400 °C in air for 2 h to reduce the mechanical stresses. The nanoindentation measurements were performed using a three-sided pyramidal Berkovich diamond indenter having a nominal edge radius of 20 nm (faces 65.3° from vertical axis) attached to a fully calibrated nanoindenter (TTX-NHT, CSM Instruments), wherein the indenter had Poisson's ratio of 0.07 and Young´s modulus of 1141 GPa.

## 3. Results and discussions

### 3.1. *Structural and micro-structural analysis* : XRD, SEM

Figures 2a and 2b illustrate the XRD patterns obtained at room temperature for the powdered samples of SG-BCZT and SS-BCZT, respectively. They exhibit the characteristic perovskite diffraction peaks, which can be indexed to the standard XRD data of tetragonal BTO having space group $P4mm$. Inset shows the Gaussian profile fitting of the {200} and {220} reflections at ~45° and ~66°, respectively. Good agreement between the observed and calculated inter-planar spacing and absence of any trace of extra peaks indicate the formation of high purity BCZT compound. Secondary phases, if any, are below the XRD detection limit. The crystallite size obtained from the Williamson-Hall analysis of XRD data is 82 nm in SG-BCZT while it is 195 nm in SS-BCZT.
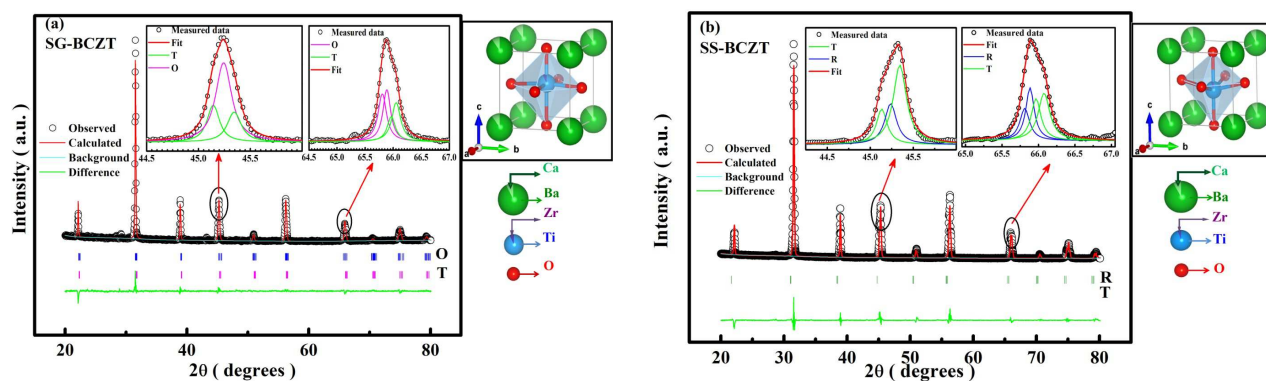
**Figure 2** Rietveld graphical output of (a) SG-BCZT and (b) SS-BCZT ceramic. The small vertical bars indicate the position of reflections (T: tetragonal; O: orthorhombic and R: rhombohedral phase). Inset: Narrow range (44.5°≤2θ≤46.0°) and (64.5°≤2θ≤67.0°) XRD patterns with Gaussian profile fitting and indicating coexistence of phases. 3D rendering of the crystal structure corresponding to the GSAS structural data obtained for the tetragonal phase, is shown next to the refined XRD profile plot.

For a detailed profile analysis, the GSAS refinement software [22] with the graphical interface EXPGUI [23] was utilized wherein Le-Bail fitting was performed prior to the crystal structural refinement. Background correction was performed using the Chebyshev polynomial of the first kind and diffraction peak profiles were fitted by the pseudo-Voigt/FCJ peak asymmetry function. Based on the final refinement results of the tetragonal phase, a 3D polyhedron model was generated for each of the sample using VESTA software [24] and are shown alongside the plots of Figs. 2 and b. The Rietveld refinement agreement factors and the phase composition are enlisted in Table 1. For the SG-BCZT sample, a combination of tetragonal, *T* (space group *P4mm*) and orthorhombic, *O* (space group *Amm*2) symmetries, converged satisfactorily thereby ruling out the presence of rhombohedral (*R*) phase at room temperature. On the other hand, refinement of SS-BCZT showed coexistence of tetragonal (space group *P4mm*) and rhombohedral (space group *R3m*) phases (Fig. 2b). As a matter of fact, the phase diagram of the BCZT system remains controversial ever since its emergence,

8

mainly because the structural distortions of perovskites are often subtle and difficult to detect. Liu *et al*. [3] reported coexistence of *R* and *T* phase. However, Keeble *et al*. [25] revealed the presence of an intermediate phase with *O* symmetry between the *R* and *T* phases in the BZT-50BCT composition. Later, Gao *et al*. [26] reported that the observed *O* phase in ref. [25] likely stemmed from the adaptive strain state of nanodomains with *T* and *R* symmetries. Still further, Haugen *et al*. [27], confirmed that the dielectric anomaly in BCZT ceramics below the Curie temperature ($T_C$) is due to the approximate volume fraction of the *R* and *T* phases ($\sim$1:1). Such discrepancies have complicated the understanding of the symmetry of the phase transition region near MPB of BZT-*x*BCT and as a consequence, reports on the co-existence of various combinations of *R*, *O* and *T*-phases for the same composition: $(Ba_{0.85}Ca_{0.15})(Ti_{0.9}Zr_{0.1})O_3$ have been reported [3,25,28-31].

Table 1 Rietveld agreement factors and phase composition of BCZT by solid state route (SS) and sol-gel method (SG). Values in parentheses are the standard deviations.

| Method | No. of variables | Agreement factors | | | Phase compositions (wt%) | | |
|---|---|---|---|---|---|---|---|
| | | $R_F^2$(%) | $R_{wp}$(%) | $\chi^2$ | Tetragonal (*P4mm*) | Rhombohedral (*R3m*) | Orthorhombic (*Amm2*) |
| SSR | 23 | 6.53 | 9.23 | 6.26 | 75.67(1) | 24.33(6) | ------ |
| SG | 30 | 5.35 | 9.36 | 3.21 | 86.1(2) | ---- | 13.9(1) |

It is quite possible that there may exist an intermediate phase bridging the *T* and *R* phases in the studied SS-BCZT as well. Perhaps, a complex interplay of lattice strains [namely, tetragonal strain {(*c*-*a*)/*a*}; rhombohedral strain {(90°-$\beta$)/90°}, where $\beta$ is the angle of the rhombohedral unit cell], forces the orthorhombic phase to evolve into an asymmetric *O*-phase with lower symmetry at narrow regions between *R* and *T* phases. This asymmetric *O*-phase, arising from a transverse instability of the lattice is difficult to be distinguished from the *R*-phase and, therefore, remains undetected by XRD [32].

9

Table 2 Unit cell and structural parameters as obtained from the Rietveld crystal structural refinements of SS and SG-BCZT. $A$-O and $B$-O represents bond length distances with $A$=Ba,Ca and $B$=Ti, Zr ; $\langle B\text{-}O \rangle$ is the average bond length ; $D$ is distortion index of the octahedron and $QE$ represents the quadratic elongation of $BO_6$ in the tetragonal phase.

| Sample | Unit cell parameters | Wyckoff position | *Atomic coordinates* | | | *Bond length* | |
| | | | $x$ | $y$ | $z$ | Vector | (Å) |
|---|---|---|---|---|---|---|---|
| SS | **Tetragonal** | Ba(1a) | 0 | 0 | 0 | $A$-O1(4×) | 2.8236(6) |
| | $a=b$=3.9836(1)Å | Ti(1b) | 1/2 | 1/2 | 0.4123 | $A$-O2(4×) | 2.6775(4) |
| | $c$=3.9995(2)Å | O1(1b) | 1/2 | 1/2 | -0.0720 | $A$-O2(4×) | 2.9752(5) |
| | $c/a$=1.004 | O2(2c) | 0 | 1/2 | 0.5294 | $B$-O1 | 1.9370(4) |
| | $Volume$=63.467 Å$^3$ | | | | | $B$-O1 | 2.0625(5) |
| | | | | | | $B$-O2(4×) | 2.0461(4) |
| | | | | | | $\langle B\text{-}O \rangle$ | 2.0307(1) |
| | | | | | | $D$ | 0.0154 |
| | | | | | | $QE$ | 1.0371 |
| | **Rhombohedral** | Ba(3a) | 0 | 0 | 0.01108 | | |
| | $a$=5.6550(8)Å | Ti(3a) | 0 | 0 | 0.4851 | | |
| | | O(9b) | 0.5183(6) | 0.4817(6) | -0.009(4) | | |
| SG | **Tetragonal** | Ba(1a) | 0 | 0 | 0 | $A$-O1(4×) | 2.8303(4) |
| | $a=b$=3.9999(1)Å | Ti(1b) | 1/2 | 1/2 | 0.520(3) | $A$-O2(4×) | 2.8668 (6) |
| | $c$=4.0093(1)Å | O1(1b) | 1/2 | 1/2 | -0.025(8) | $A$-O2(4×) | 2.7970(5) |
| | $c/a$=1.0023 | O2(2c) | 1/2 | 0 | 0.487(7) | $B$-O1 | 2.1895(8) |
| | $Volume$=64.147 Å$^3$ | | | | | $B$-O1 | 1.8198(3) |
| | | | | | | $B$-O2(4×) | 2.0042(5) |
| | | | | | | $\langle B\text{-}O \rangle$ | 2.0044(1) |
| | | | | | | $D$ | 0.0308 |
| | | | | | | $QE$ | 1.0057 |
| | **Orthorhombic** | Ba(2a) | 0 | 0 | 0 | | |
| | $a$=3.9874(1)Å | Ti(2b) | 1/2 | 0 | 0.516(9) | | |
| | $b$=5.6751(1)Å | O1(2a) | 0 | 0 | 0.491(3) | | |
| | $c$=5.6901(1)Å | O2(4e) | 1/2 | 0.256(5) | 0.236(7) | | |

A comprehensive list of the crystal structure parameters including the refined lattice parameters, unit cell volume, tetragonality, atomic positions and bond lengths of the studied

ceramics are enlisted in Table 2. The observed elongation of the unit cell along the *c*-axis and deviation of the tetragonality (*c/a*) ratio from unity indicates an average relative displacement of titanium ions along the *c*-axis from its centrosymmetric position in the unit cell and, thereby, confirms the presence of the ferroelectric phase [33]. It is also noticed that the difference between the two apical *B*-O1 bond distances is greater in SG-BCZT sample (*cf.* Table 2) implying a larger octahedral distortion of the $BO_6$ cage [30], which is realised through its higher distortion index, *D*. Further, the unit cell lattice parameters (and unit cell volume) for the tetragonal phase  is larger in the SG-BCZT sample as compared to SS-BCZT (*cf.* Table 2). Additionally, the tetragonal strain defined as {(*c-a*)/*a*}, decreases from 0.4% in SS-BCZT to 0.2% in SG-BCZT. The value obtained for SG-BCZT is about 1/5 of the value reported in BTO (1%) single crystals [34]. These dimensional changes including tetragonality can be attributed to the effect of internal stress on the crystal structure that develops during cooling across the ferroelectric phase in a ceramic [35]. Generally, larger grains in a coarse-grained ceramic allows for the growth of a domain structure such that it provides a three dimensional compensation for homogenous stress [18]. Whereas, in ceramics with smaller sized grains, only partial internal stress relief within the grains is allowed, thereby causing development of inhomogeneous stress at the grain boundaries. For the studied samples, it is observed in the FESEM images (Figure 3) that grains with an estimated average size ~1.48±1.1 $\mu$m were obtained by sol gel technique (SG-BCZT, Fig. 3a), while comparatively much larger grains having an average size ~27.61±9.13 $\mu$m were obtained by conventional solid state sintering method (SS-BCZT, Fig. 3b). In the fine-grained SG-BCZT, therefore, the stresses due to the ferroelectric deformation becomes more difficult to be released, resulting in some unrelieved stresses to remain inside the grains [18]. This uncompensated stress is expected to reduce the tetragonal distortion [35], as indeed observed in SG-BCZT.

With regard to the micro-structural features of SG-BCZT sample (Fig. 3a), a few isolated pores are observed on the grain boundaries in the otherwise well developed microstructure.

11

While for coarse-grained SS-BCZT, a dense microstructure with well-defined grain boundaries is observed. The grain-size distribution for both the samples is shown in the inset of their respective SEM images. The apparent bulk density value obtained for SS-BCZT was ~5.53 g/cm$^3$ which is ~95% of the theoretical density (5.82 g/cm$^3$) while for SG-BCZT, it was ~5.19 g/cm$^3$ which is ~90% of the theoretical density (5.76 g/cm$^3$).
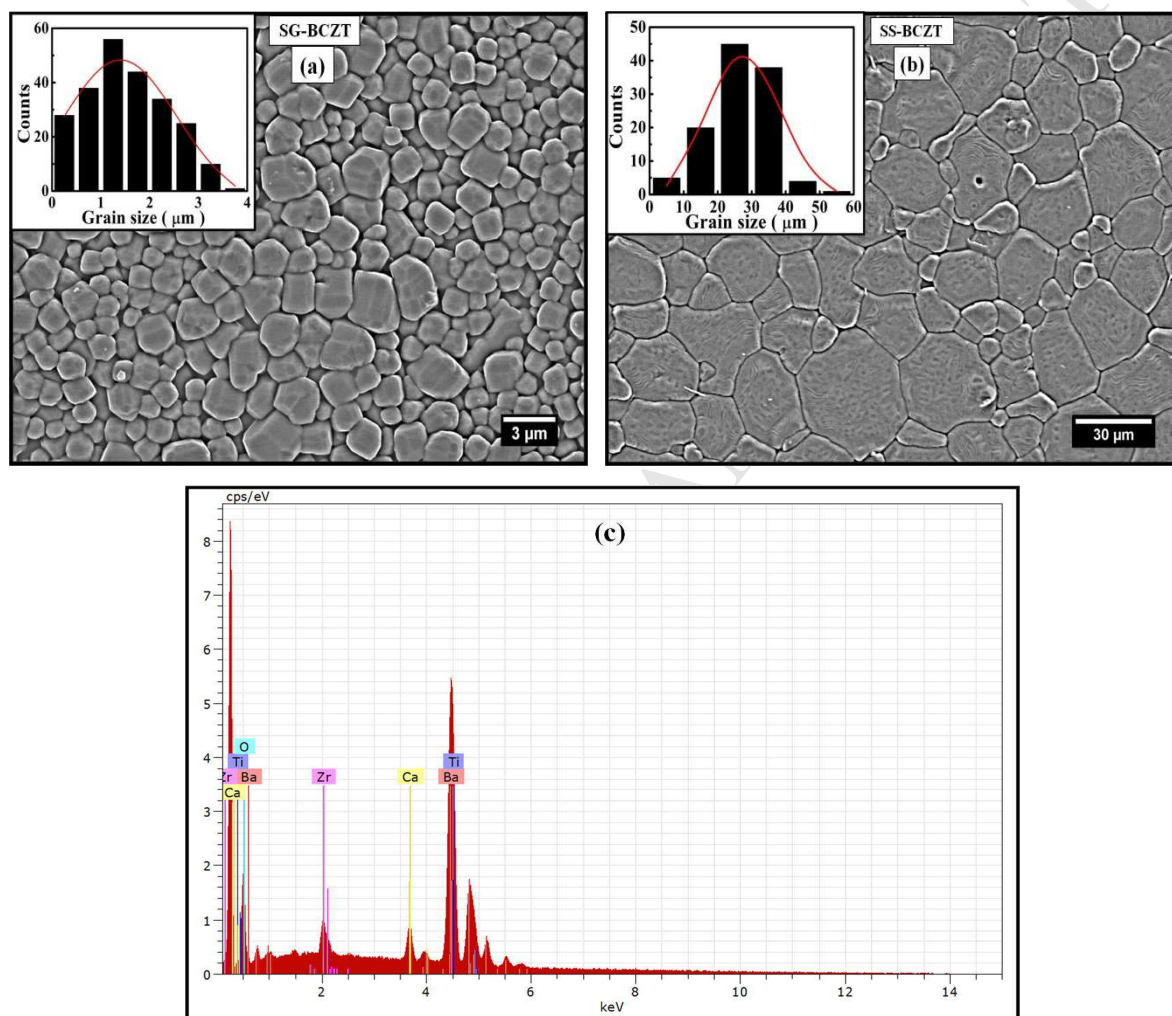


**Figure 3** Scanning electron micrographs of the sintered surfaces of (a) SG-BCZT and (b) SS-BCZT samples. Inset: Grain size distribution with Gaussian fitting. (c) SEM-EDS of SG-BCZT sample.

To ascertain the composition, EDS mapping was performed and the corresponding elemental distribution pattern is shown in Fig. 3c (for SG-BCZT). Detection of constituent metal elements Ba, Ca, Ti, Zr is evident in the EDS image. The obtained atomic percentage of

elements is in good approximation to the expected ratios. The values of measured (and theoretical) atomic percentage of Ba : Ca : Ti : Zr in the SG-BCZT sample is 41.9 (42.5): 7.14 (7.5): 46.08 (45): 4.12 (5).

### 3.2. *Temperature dependent dielectric studies: dielectric constant and loss tangent*

Figure 4a displays the variation of dielectric constant as a function of temperature obtained for SS- and SG-BCZT samples at 100 kHz. A comparison of results reveal higher Curie temperature along with lower and broadened permittivity maxima in SG-BCZT sample. The possible influence of grain size in rendering these modifications is discussed in the present section.
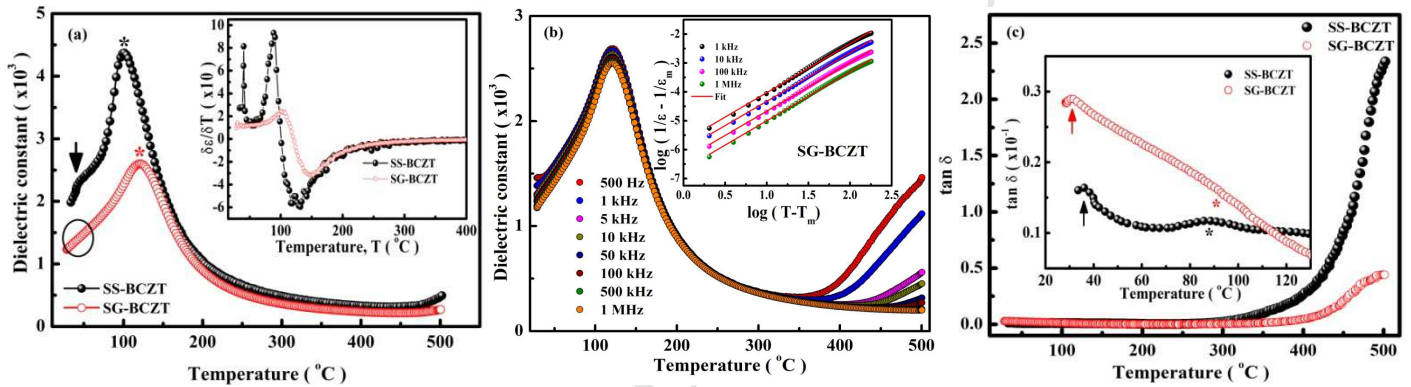


**Figure 4** (a) Comparison of temperature variation of dielectric constant in SS- and SG-BCZT samples. Inset: Derivative of relative dielectric permittivity as a function of temperature. (b) Temperature dependence of dielectric constant at various frequencies in SG-BCZT. Inset shows fitting with Eq. (1) to evaluate degree of diffuseness. (c) Loss tangent variation with temperature. Inset shows enlarged view between 20-130 °C.

In agreement with the general behaviour reported in literature for ceramics with smaller grains [36], the dielectric curve exhibits a relatively broadened maximum in the SG-BCZT sample. However, this transition at the dielectric maximum is only rounded without any frequency dispersion (Fig. 4b), negating any relaxor characteristic of the diffused phase transition. To evaluate the degree of diffuseness of the *ferro-para*electric phase transition, the following modified empirical expression was employed [37]:

13

$$\frac{1}{\varepsilon} - \frac{1}{\varepsilon_m} = \frac{(T - T_m)^\gamma}{C'}, \qquad\qquad (1)$$

where $\varepsilon_m$ is the maximum permittivity, $T_m$ is the permittivity maximum temperature while $\gamma$ and $C'$ are constants. The quantitative parameter that determines the degree of relative broadness/diffuseness in the dielectric spectra is given by the diffuseness exponent ($\gamma$) with values varying from 1 for a normal ferroelectric to 2 for an ideal relaxor ferroelectric. Logarithmic plots based on Eq. 1 are shown in the inset of Fig. 4b (SG-BCZT sample). A linear relationship was obtained for various frequencies in 1 kHz-1 MHz range. The critical exponent, $\gamma$, as obtained from the slope, yielded 1.69 and 1.57 for SG- and SS-BCZT samples, respectively. The plausible cause of broadness or diffusiveness could be due to the compositional fluctuation and/or structural disordering in the arrangement of cation(s) in one or more crystallographic sites causing a microscopic heterogeneity in the compound [36,38,39]. Besides compositional fluctuation, the internal stresses caused by the grain boundaries in the smaller grain sample can also promote diffuseness [36,38,39]. This explains the higher $\gamma$ value in SG-BCZT sample as compared to the SS-BCZT sample.

In addition, it is also observed that the relative permittivity in the SG-BCZT ceramic sample is markedly reduced as compared to the coarse-grain sample (Fig. 4a). This observation is in accordance with reported results for the BCZT composition and other ferroelectric systems, wherein the permittivity statistics is strongly grain-size dependent and shows a systematic decrease with decreasing grain size [19, 38,40-42]. The "*dilution effect*" associated with the presence of low permittivity nonferroelectric grain boundaries, often termed as the "*dead layers*", causes a drop in permittivity values [43-44]. Therefore, a decrease in the grain size will result in not only an increase in fraction of low permittivity regions but also on the distribution of internal stresses on the grains. This will inevitably lead to an overall decrease in the dielectric constant of the sample, as observed in SG-BCZT.

As far as the *ferro-ferro* and *ferro-para*electric phase transitions are concerned, both the samples show distinct signatures. Based on our refinement results and as indicated in Refs.

14

[3,4,29,39], the transition near 42 °C in SS-BCZT sample is the *R-T* phase transition ($T_{R-T}$). On the other hand, in the SG-BCZT sample, a barely discernible, highly diffused and broadened tail-like feature is observable just above room temperature (encircled in the figure 4a). To clarify whether it really represents a phase transition, the first derivative of relative permittivity was plotted *w.r.t.* temperature (inset of Fig. 4a). A jump/anomaly in derivative near room temperature indicates the *O-T* phase transition ($T_{O-T}$) in the SG-BCZT sample. The *ferro-para*electric transition (tetragonal→cubic, marked by ´*´ in Fig. 4a), is distinctly noticeable in both the samples. The respective Curie temperature, $T_c$, of SG-BCZT and SS-BCZT samples, as estimated from permittivity peak position are 121 °C and 102 °C, respectively. This observation of an increase in $T_c$ with decreasing grain size is consistent with previous reports [18,19,38,40,42,45]. In addition, intrinsic factors like the cell distortion parameter and the cell volume is also believed to have an important effect on phase transition temperature [23,46]. Zhang *et al.* [46] in their study on $Ba_xSr_{1-x}TiO_3$ established that variation of $T_c$ can be attributed to an effective volume effect of the unit cell (quantitatively related to lattice parameter $\gamma = \sqrt[3]{a^2 c}$) and concluded that $T_c$ increases as the unit cell enlarges. Similarly, hydrostatic pressure experiments on BTO confirmed that the Curie temperature decreases linearly with hydrostatic pressure (*i.e.* shrinking unit cell) [47-48]. Still further, Qi *et al.* [49] utilized first-principle density-functional theory calculations to correlate tetragonality (*c/a*) and $T_c$ and claimed that with a decrease in *c/a* there is an increase in $T_c$. Investigation on the solid solution, $xPbTiO_3$-$(1-x)BiScO_3$ and $xBiMg_{1/2}Ti_{1/2}O_3$-$(1-x)PbTiO_3$ confirmed this qualitative relationship [50-51].

In the present case:

(a) the unit cell volume in terms of lattice parameter $\gamma = \sqrt[3]{a^2 c}$, is 4.0030 Å for SG-BCZT sample which is higher than that for SS-BCZT sample (3.9889 Å) and

(b) the ratio *c/a* is lower for SG-BCZT sample.

Based on the above observations, we believe that reduction in tetragonality and simultaneous expansion of unit cell volume produces an effect that shifts the Curie temperature to a higher temperature as observed in SG-BCZT sample.

Temperature dependence of tangent loss (tan δ) for both the samples is depicted in Fig. 4c. The loss tangent behaviour in the low temperature range is magnified in the inset. Anomalies in loss tangent curve are noticeable near both the phase transitions: *ferro-ferro* (marked by `arrow´) and *ferro-para*electric (marked by `*´). A comparison of the loss tangent curve brings forth the contrasting character in different temperature regions. For the lower temperature range (below $T_c$), loss tangent is higher in SG-BCZT, while for very high temperatures (>350 °C) the loss tangent is significantly lower in SG-BCZT. This behaviour may be understood in terms of the contribution from domain walls to the dielectric loss. One of the major sources of dielectric loss arises from the irreversible domain wall motion [52]. Since there is a higher density of wall pinning centers in fine-grained SG-BCZT ceramic, the loss response is greater than that in SS-BCZT sample. While above $T_c$, owing to the dissolution of domains there is no contribution from the wall motion which explains the drop in loss. Additionally, for the temperature range ≥ 350 °C, it is possible that the higher grain-conductivity in SS-BCZT (see more in the following sections), is playing a dominant role in increasing the loss tangent values.

### 3.3a. *Ferroelectric and piezoelectric studies*

Fundamentally, the electromechanical response in polycrystalline ferroelectric ceramics comprises several contributions, which are typically categorized into two major groups, namely: (i) *intrinsic contribution* that refer to the reversible response of inherent lattice distortion *w.r.t.* external field (electric and/or mechanical),and (ii) the *extrinsic contribution*, that are primarily, but not solely due to the motion of ferroelectric-ferroelastic (non-180°) domain walls, which could be either reversible or irreversible [53-55]. The difference between the electromechanical responses of the small- and coarse-grained ceramics is

generally attributed to the dynamics of the extrinsic contribution that are dominant well below the transition temperature. According to the Avrami model proposed by Orihara *et al.* [56], the proportion of grains contributing in polarization reversal increases with increasing grain size. In fine-grained ceramics, although the domain density increases, however there is a decrease in the extrinsic response owing to an increase in the effective elastic stiffness of domain walls through the domain-wall–domain-wall interaction [57]. It is also believed that the grain boundaries contribute as additional pinning centers for the moving walls. Clamping of domain walls at the grain boundaries makes the domain reorientation more difficult and constrains the domain wall motion. Consequently, (a) the increase in elastic stiffness and (b) higher volume of grain boundaries, affect the contribution of the extrinsic mechanism to the functional properties in ways such that:

(i) the value of remnant polarization becomes smaller (because of the reduction of the achievable aligned domain), and

(ii) the effective dielectric and piezoelectric coefficients reduces (because of the decrease in domain wall mobility).

In agreement with these aforementioned arguments, we observed a significant drop in remnant ($P_r$), saturation polarization ($P_s$) and $d_{33}$ values for the fine-grained SG-BCZT samples.

The room temperature ferroelectric switching behaviour of the samples were investigated in terms of polarization-electric field (P-E) hysteresis loops at a driving frequency of 1 Hz (Fig. 5). The $P_s$ and $P_r$ values are ~13.8 $\mu$C/cm$^2$ and ~10.8 $\mu$C/cm$^2$ for SS-BCZT sample which is much higher than that achieved in SG-BCZT showing values ~4 $\mu$C/cm$^2$ and ~2 $\mu$C/cm$^2$, respectively. The coercive field, $E_c$ estimated from the loops are ~5.8 kV/cm for SS- and ~9.34 kV/cm for SG-BCZT. The increase in effective coercive field in SG-BCZT also reflects the grain size influence; since the presence of higher volume of grain boundaries with reduced permittivity increases $E_c$ [58]. The insets of Fig. 5 illustrate the evolution of

17

ferroelectric hysteresis loops of the studied samples measured under increasing electric field amplitude at a fixed frequency of 1 Hz. In both samples, the P-E loops show dependence on the field amplitude in a way such that the $P_r$ and $E_c$ increase with increasing field amplitude, though the rates of increase are different to one another. However, the increase in $P_r$ was noted to be less than 2% and almost constant beyond applied electric field amplitude of 30kV/cm (SS-BCZT) and 40kV/cm (SG-BCZT).
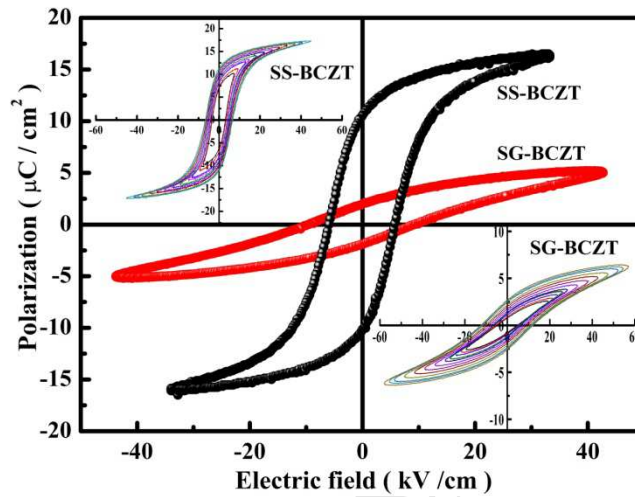


**Figure 5** Ferroelectric hysteresis loops in SG- and SS-BCZT ceramic samples. Inset shows evolution of loops with increasing electric field amplitude.

In addition to the influence of extrinsic contribution, the observed polarization behaviour can also be understood in terms of inherent lattice distortion effects. In the framework of the Landau-Ginzburg-Devonshire thermodynamic theory of ferroelectrics, it is possible to relate, at least qualitatively, the variation of tetragonality and the ferroelectric properties in a system. The tetragonal distortion of the lattice, $\eta$ is proportional to the square of the spontaneous polarization, $P_s$ [43,59]

$$\eta = \frac{c}{a} - 1 = kP_s^2, \qquad (2)$$

where $k$ is the difference $(Q_{11}-Q_{12})$ of the electrostrictive coefficients. According to equation (2), a change in lattice deformation determines a variation of polarization. It is, therefore,

18

natural that the lower value of $\eta$ as observed in the SG-BCZT sample (Table 2) may result in lower $P_s$ values.

The longitudinal piezoelectric charge coefficient, $d_{33}$ values for SS- and SG-BCZT samples obtained are 345 pC/N and 39 pC/N, respectively. The value in coarse-grained SS-BCZT sample is therefore nearly 9 times higher than that in SG-BCZT sample. Such low values of $d_{33}$ for BCZT ceramics having small grains have been previously reported [12,14,45]. The observance of low piezoelectric response in small grain SG-BCZT ceramic can be associated with the increase in elastic stiffness and progressive hindrance to domain wall movements. While in SS-BCZT with larger grains, the domain-wall displacement will be easier and so its contribution to $d_{33}$ will be significantly larger, thereby enhancing the electromechanical response. Moreover, it is well known that the remanent polarization is proportional to piezoelectric constant as per the thermodynamic relation [60]:

$$d_{33} = 2Q_{11} \cdot P_r \cdot \varepsilon_{33} \qquad (3)$$

where $Q_{11}$ represents the electrostrictive coefficient and $\varepsilon_{33}$ is the dielectric constant. According to Eq. (3), $d_{33}$ will follow similar trend as that of $P_r$. Since SG-BCZT has lower $P_r$ value, it is expected to show inferior piezoelectric characteristics in comparison with SS-BCZT. Moreover, the retention of internal stresses in fine-grained ceramic may hinder the domain switching process [33], thereby causing difficulty in poling and the ensuing lower value of piezoelectric coefficient in SG-BCZT compound.

**3.3b. *Domain imaging: Piezoresponse Force Microscopy (PFM)***

Room temperature local-area piezoresponse investigations were conducted to image the domain configuration and domain sizes in the studied ceramics to correlate with the observed macroscopic properties.
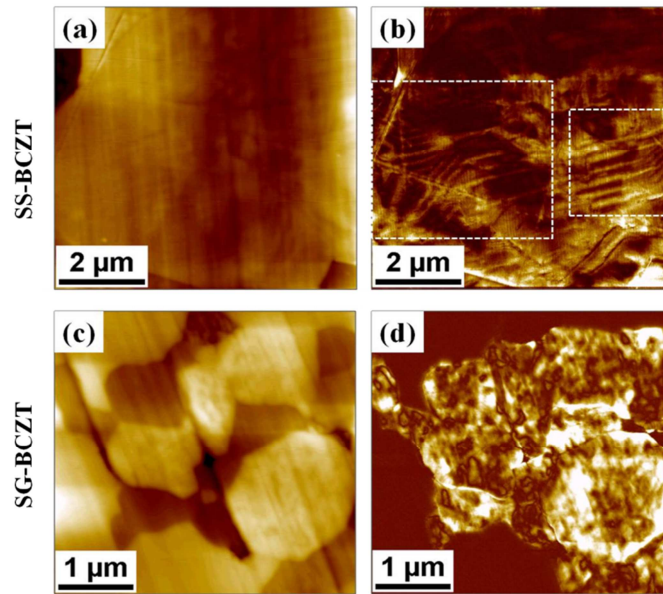
19

**Figure 6** Piezoresponse images showing the domain configuration. (a,c) Topography and (b,d) PFM amplitude.

Figures 6a and c show the topography of polished surfaces of un-poled and annealed SS- and SG-BCZT samples, respectively. The corresponding PFM amplitude images are shown in Figs. 6b and d. Wedge shaped domains consisting of fragmented lamellar sub-domains overlapped with watermark areas are observed in the coarse-grained SS-BCZT sample (Fig. 6b). The average period of lamellar domain is 250±90 nm. In contrast, the domain structure in SG-BCZT ceramic revealed irregularly distributed nano sized fractal-like domains. It must however be noted that, though domain wall contrast was observed in PFM amplitude signal, the domain width of the nanodomain structure could not be estimated directly owing to the limited resolution of PFM. A rough estimate of the domain width by autocorrelation function approach [61] yielded an average size of 150±60 nm. It is therefore evident from the domain configuration in SG-BCZT sample, that the extrinsic contribution to piezoelectric properties will be negligible and thus supports the observance of inferior $d_{33}$.

**3.3c.** *Mechanical properties: Nanoindentation*

Though piezoelectric charge coefficient is one of the most important parameter, which determines the actuator performance, it is also necessary to study the mechanical properties.

20

Parameters such as Young's modulus, which determines the conversion of the strain to force delivered by the actuator; hardness and fracture toughness which decide the reliability during actuator operation, are therefore important as well.
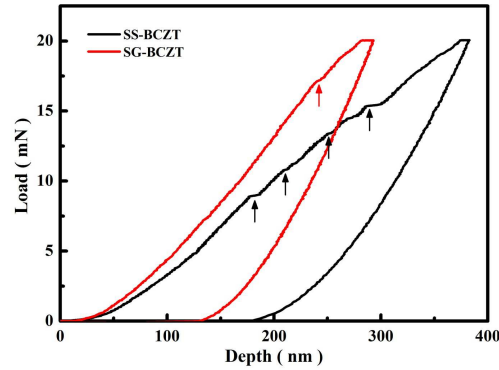


**Figure 7** Load-displacement curves of indentations made on SG- and SS-BCZT ceramics. Pop-in events are marked by arrow.

Figure 7 depicts the typical load-unload data curve versus indentation-penetration depth taken at maximum load of 20 mN. Basically, a total of 7 indents were made with varying peak loads in the range 5 - 75 mN with an approach speed of 2000 nm/min. The loading and unloading rate was maintained at 20 mN/min with dwell time of 10 seconds. The mechanical response, as observed, is different for the studied ceramic samples. It is purely elastic for loads of 17 mN and below in SG-BCZT, with contributions from plastic deformation apparent at higher loads. While in SS-BCZT, plastic deformations appears for loads higher than 9 mN. The pop-in events or "kinks" in the loading curves (marked by arrow in the figure 7) are related to the elastic to elastic-plastic transition regime, and are also associated with the nucleation of plastic deformation due to dislocations, slips and cracks [62].

Young's modulus and hardness were extracted from the unloading curve using the standard Oliver and Pharr method [63]. The values of Young's modulus and hardness for SS-BCZT are 117.9 GPa and 14.1 GPa, respectively. While for SG-BCZT, the respective values are 158.3 GPa and 20.5 GPa. The results are in accordance with literature which emphasizes that materials with lower Young´s modulus would have higher piezoelectric coefficients [45, 64].

21

**4a.** *Impedance spectroscopy***:** *applicability of the brick layer model*

Complex impedance spectroscopy was utilized to quantify the resistance ($R$) and capacitance ($C$) associated with the electrically different active regions, namely grain ($g$) and grain-boundary ($gb$). In further discussions, we shall use the following notations: $R_g$ (grain resistance), $C_g$ (grain capacitance) and $R_{gb}$ (grain boundary resistance), $C_{gb}$ (grain boundary capacitance). These measured electrical parameters can be correlated with the sample microstructure based on the most widely accepted brick layer model (BLM) [65-66]. According to BLM, the material is assumed to consist of an array of cubic shaped grains with edges of length $d_g$, separated by flat grain boundaries of thickness $\delta_{gb}$ where $\delta_{gb} \ll d_g$. By assuming that the grain boundary is considerably more resistive than the grain interior, it is possible to derive expressions relating the experimentally obtained electrical properties of the material *viz.* $R_{gb}$, $C_{gb}$ and $C_g$ to the microstructural parameters [66]. In general, few issues like significant porosity, secondary phases or very inhomogeneous grain size distributions may lead to artefacts in the impedance spectra, thereby limiting the applicability of the BLM in estimation of the grain boundary properties. However, the disparity scarcely exceeds a factor of two [67].

Figures 8a and b, show the complex impedance plane plots of SG- and SS-BCZT samples respectively measured at various temperatures in the frequency range from 100 Hz to 1 MHz. In both samples, grain interior and grain boundary arcs are observed to be well resolved in the impedance spectrum. By fitting the data (Z-view fitting software, v3.2c, Scribner Associates, Inc.), to an equivalent circuit consisting of two resistors in series each shunted by a constant phase element (as shown in inset of Fig. 8b), the values of $R_g$, $C_g$, $R_{gb}$ and $C_{gb}$ were obtained (enlisted in Table 3). In both samples, $C_{gb}$ is found to be higher than $C_g$. Permittivity values from the bulk capacitance data can be treated approximately as true permittivity, because of the negligible thickness of GB layers (typically of a few tens of nm) in relation to the grain size [42,68]. The calculated values are tabulated in Table 3 and agrees

well with the permittivity data obtained experimentally (Fig. 4a). Relaxation time, $\tau_i = R_i C_i$ where $i$ corresponds to either $g$ or $gb$, was also evaluated.
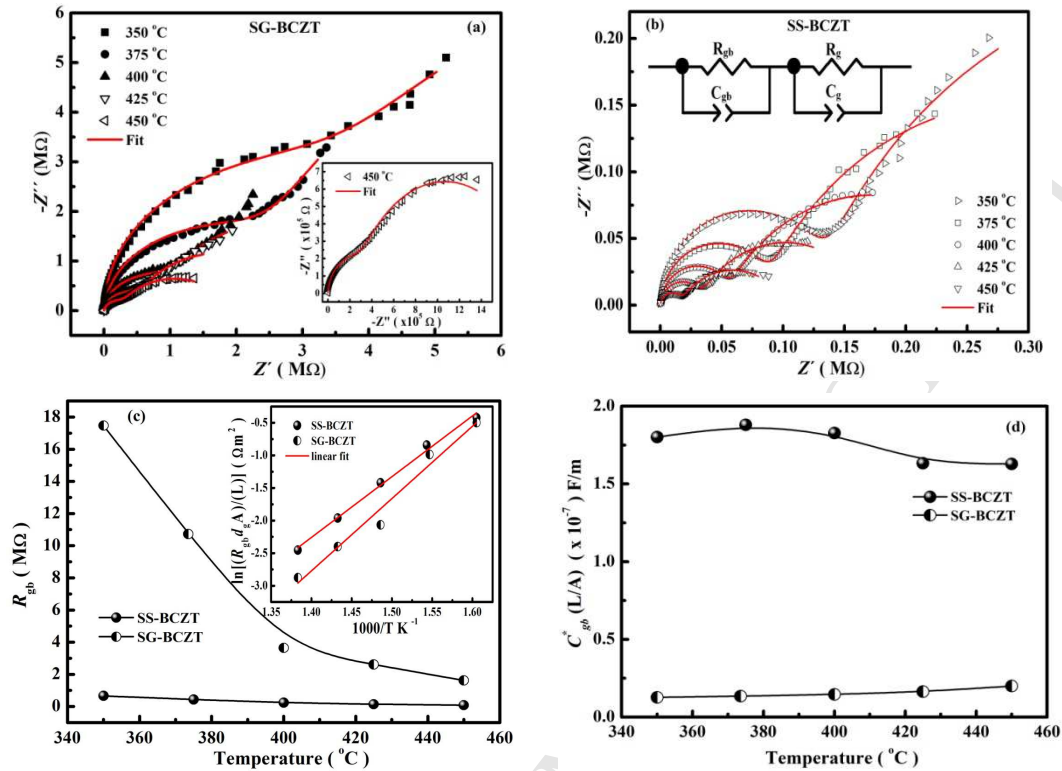


**Figure 8** Complex impedance plots for (a) SG-BCZT and (b) SS-BCZT samples. Inset in (a) shows the spectrum at 450 °C for clarity in determining the two arcs, whilst inset in (b) shows the equivalent circuit. (c) Comparison of grain boundary resistance values between SS- and SG-BCZT samples. Inset shows the logarithmic behaviour of $R_{gb}$ with temperature with corrections for differences in area to thickness ratio (A/L), and differences in average grain size $d_g$ (d) Comparison of grain boundary capacitance values (with corrections for differences in thickness to area ratio (L/A)) between SS- and SG-BCZT samples at various temperatures.

Figure 8c compares the $R_{gb}$ values in the studied BCZT samples. The effect of grain size on $R_{gb}$ is consistent with the trend predicted by the BLM, wherein the grain boundary resistance is expected to increase in samples with smaller grains owing to an increase in the volume fraction of grain boundaries across the sample [65]:

23

$$R_{gb}\frac{A}{L} = \frac{(\rho_{gb}\cdot\delta_{gb})}{d_g}, \qquad (4)$$

In Eq. (4), $A$ and $L$ are electrode area and sample thickness, respectively; while $\rho_{gb}$ is the grain boundary resistivity and $d_g$ is the average grain size. The ratio $L/d_g$ represents the number of grain boundaries across the sample. Though the GB effect on $R_{gb}$ is noticeable, however, the accurate applicability of the BLM can be assessed by analysing the temperature dependence of $R_{gb}d_gA/L$, as shown in the inset of Fig. 8c. Appropriate corrections for differences in area to thickness ratio ($A/L$), and differences in average grain size $d_g$ were taken into account. Ideally, as per BLM (and assuming similar GB thickness in both samples), the values of $R_{gb}d_gA/L$ should have been nearly independent of grain size and their logarithmic behaviour should have obeyed a common dependence *w.r.t.* $1/T$. However, it is noted that the activation energy value obtained from the slope is different for the samples: 0.88eV (SS-BCZT) and 0.99eV for SG-BCZT sample. This discrepancy could be the result of the wide grain size distribution in SS-BCZT sample, whose microstructure comprises of both small and very large grains (inset of Fig. 3b). In such a scenario, the current lines would prefer to make detours across the largest grain in order to minimise the number of boundaries effectively crossed and follow a path of least resistance. Such diversions of current paths in the microstructure is likely to lower the grain boundary resistance (relative to the BLM), resulting in divergence of the effective true activation energy of the GB resistivity [67-68], as in case of SS-BCZT.

One can also envisage a trend for the grain size effects on GB capacitance $C_{gb}$, which is expected to increase with an increase in the average gain size [65,68]:

$$C_{gb}\frac{L}{A} = \frac{(\varepsilon_o\cdot\varepsilon_{gb}\cdot d_g)}{\delta_{gb}}, \qquad (5)$$

In Eq. (5), $\varepsilon_o$ and $\varepsilon_{gb}$ are the dielectric permittivity of vacuum and grain boundary, respectively. Fig. 8d compares the $C_{gb}$ values (corrected to sample geometry) for both samples. As expected, the grain boundary capacitance of coarse-grained sample is about an

order of magnitude higher than that of small grained SG-BCZT throughout the studied temperature regime.

Table 3 Impedance fitting results- grain resistance ($R_g$) and capacitance ($C_g$); grain boundary resistance ($R_{gb}$) and capacitance ($C_{gb}$) along with corresponding grain ($\tau_g$) and grain boundary ($\tau_{gb}$) relaxation times, respectively. Approximate grain permittivity ($\varepsilon_g$) values estimated using Eq. 6. For comparison, dielectric constant ($\varepsilon_r$) values obtained from dielectric measurement (Fig. 4a) is also mentioned.

| Temperature | $R_g$ | $R_{gb}$ | SS-BCZT $C_g$ | $C_{gb}$ | $\tau_g$ | $\tau_{gb}$ | $\varepsilon_g$ | $\varepsilon_r$ |
|---|---|---|---|---|---|---|---|---|
| ( °C ) | (kΩ) | (kΩ) | (pF) | (nF) | ($\mu$s) | (ms) | | |
| 350 | 126.34 | 661.26 | 138.1 | 6.62 | 17.45 | 4.38 | 424 | 386 |
| 375 | 82.37 | 434.61 | 127.8 | 6.91 | 10.53 | 3.0 | 392 | 355 |
| 400 | 51.99 | 243.64 | 119.16 | 6.72 | 6.19 | 1.64 | 366 | 329 |
| 425 | 31.12 | 141.64 | 115.37 | 6.0 | 3.59 | 0.85 | 354 | 317 |
| 450 | 15.81 | 86.63 | 114.82 | 5.99 | 1.81 | 0.52 | 352 | 319 |

| Temperature | $R_g$ | $R_{gb}$ | SG-BCZT $C_g$ | $C_{gb}$ | $\tau_g$ | $\tau_{gb}$ | $\varepsilon_g$ | $\varepsilon_r$ |
|---|---|---|---|---|---|---|---|---|
| ( °C ) | (kΩ) | (MΩ) | (pF) | (nF) | ($\mu$s) | (ms) | | |
| 350 | 3231.6 | 17.47 | 74.51 | 0.37 | 240.79 | 6.43 | 290 | 280 |
| 375 | 2277 | 10.72 | 93.35 | 0.39 | 212.57 | 4.18 | 363 | 255 |
| 400 | 1021.9 | 3.64 | 77.30 | 0.42 | 78.99 | 1.53 | 301 | 234 |
| 425 | 525.24 | 2.61 | 79.14 | 0.47 | 41.57 | 1.24 | 354 | 222 |
| 450 | 271.83 | 1.62 | 91.1 | 0.58 | 24.76 | 0.93 | 354 | 217 |

## 4b. *Grain and grain boundary conductivities*

The two microelements, namely, bulk grain and grain boundary, contribute to the conduction process that affects the electrical properties. The total bulk grain conductivity comprising

contributions from the mobile ionic and/or electronic charge carriers can be expressed as [69]:

$$\sigma_g = ne\mu_e + pe\mu_h + 2[V_o^{\bullet\bullet}]e\mu_V \qquad (6)$$

where $\mu_e$, $\mu_h$ and $\mu_V$ represent electron-, hole- and oxygen vacancy mobilities, respectively. Cation vacancies are relatively immobile, so that their contribution to electrical conduction is almost negligible. Oxygen vacancies are significantly more mobile and may give rise to a dominant ionic conductivity detectable even at room temperature [70]. The electronic charge carriers (holes and electrons), have relatively small mobilities (*e.g.* $\mu_h = 0.1$ cm$^2$/Vs at 1223 K) that decrease with increasing temperature [71].

Grain boundaries have a pronounced effect on electrical conductivity, too, since they are believed to act as source and sinks for point defects. The charge transport in GB region is influenced by the space-charge depletion regions (formed on both sides of the GB core) and diffusion along the core region [72].

A comparison between the $\sigma_{gb}$ and $\sigma_g$ of the respective samples is presented in Figure 9. The observed Arrhenius-like decrease of GB resistance or the linear increase in grain boundary conductivity, $\sigma_{gb}$ is primarily due to the fact that the potential barrier height in the GB region remains almost constant in the temperature regime under consideration [70]. It can also be noticed that the $\sigma_{gb}$ is lower in magnitude than $\sigma_g$ in both samples, implying that the current path is predominantly through grains and across grain boundaries. The activation energy associated with the GB conductivity ($E_a^{gb}$) and grain conductivity ($E_a^g$) extracted from the slope of the Arrhenius plots are: 0.92 eV and 0.90 eV for SS-BCZT and 1 eV and 0.96 eV for SG-BCZT sample. Based on the activation energy values and the considered temperature range, it is believed that the ionic species primarily contributing to the grain conductivity are the intrinsic defects, like $V_o^{\bullet\bullet}$ [73]. Cation vacancies like titanium and/or barium vacancies, if present, are relatively immobile. Ti vacancy has a prohibitively high activation energy of migration (~15 eV), while for barium vacancies ($V_{Ba}^{''}$), it is ~2.8 eV [74]. Also, the most

26

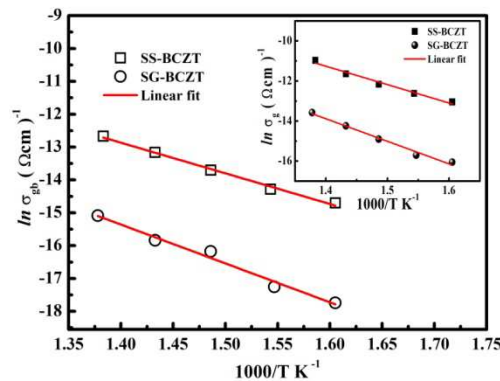likely constituents in the GB core region are the accumulated oxygen vacancies which contribute to $\sigma_{gb}$.



**Figure 9** Comparison of Arrhenius plots of $\sigma_{gb}$ in SG- and SS-BCZT samples. Inset shows the comparison of grain conductivity ($\sigma_g$) between SS- and SG-BCZT samples.

Moreover, the effect of grain boundary volume fraction is also evident in the observed behaviour. Since the fine-grained SG-BCZT ceramic possesses a higher volume fraction of grain boundaries, the $\sigma_{gb}$ is lower in magnitude as compared to the coarse-grain SS-BCZT [75]. With respect to the grain conduction process, SG-BCZT shows lower $\sigma_g$ as compared to SS-BCZT sample (inset Fig. 9). This result can be correlated with the loss tangent behaviour (Fig. 4c, Section II). Given that the activation energy associated with grain conduction process is lower in SS-BCZT than that of SG-BCZT, it implies that motion of charge carriers (oxygen ions in this case) is comparatively easier in SS-BCZT sample. This results in a higher $\sigma_g$ in SS-BCZT sample (inset Fig. 9), suggesting a possible higher concentration of $V_o^{\bullet\bullet}$ (as per Eq.6). It is therefore reasonable to deduce that the higher tangent loss in SS-BCZT sample for temperatures greater than 350 °C, is due to higher oxygen vacancies.

**5. Conclusions**

$(Ba_{0.85}Ca_{0.15})(Zr_{0.10}Ti_{0.90})O_3$ bulk ceramics were obtained by sol-gel and solid state reaction methods. The different preparation techniques rendered a microstructure with significant difference in their average grain size. Sol-gel derived SG-BCZT sample showed an average

27

grain size of ~1.5 $\mu$m, while coarse grains with average grain size 27$\mu$m were obtained in SS-BCZT sample prepared by solid state method. The effect of this grain size difference was realised in the results of dielectric, ferroelectric, piezoelectric and impedance properties. The decrease in grain size and concomitant increase in grain boundary density is believed to enhance diffuseness and lowering of the dielectric maximum in SG-BCZT. A drop in both ferroelectric and piezoelectric properties is observed in SG-BCZT, due to enhanced internal stresses caused by the large volume fraction of grain boundaries on the grains and progressive hindrance of the domain wall movements. The SG-BCZT sample showed higher elastic stiffness (Young´s modulus: 158.3 GPa) as compared to 117.9 GPa in SS-BCZT. Influence of grain size effects were noted in complex impedance spectroscopy results as well. Higher grain boundary (GB) resistance, lower GB capacitance and lower conductivity were observed in SG-BCZT as compared to coarse-grained SS-BCZT sample.

## Acknowledgements

## References

[1] A. von Hippel, Ferroelectricity, domain structure, and phase transitions of barium titanate, Rev. Mod. Phys. 22 (1950) 221-237.

[2] L.S. -Seveyrat, A. Hajjaji, Y. Emziane, B. Guiffard and D. Guyomar, Re-investigation of synthesis of $BaTiO_3$ by conventional solid-state reaction and oxalate coprecipitation route for piezoelectric applications, Ceram. Int. 33 (2007) 35-40.

[3] W. Liu and X. Ren, Large piezoelectric effect in Pb-Free ceramics, Phys. Rev. Lett. 103 (2009) 257602-1-4.

[4] I. Coondoo, N. Panwar, H. Amorín, M. Algueró and A.L. Kholkin, Synthesis and characterization of lead-free $0.5Ba(Zr_{0.2}Ti_{0.8})O_3$-$0.5(Ba_{0.7}Ca_{0.3})TiO_3$ ceramic, J. Appl. Phys. 113 (2013) 214107-1-6.

[5] Y. Tian, L. Wei, X. Chao, Z. Liu and Z. Yang, Phase transition behavior and large piezoelectricity near the morphotropic phase boundary of lead-free $(Ba_{0.85}Ca_{0.15})(Zr_{0.1}Ti_{0.9})O_3$ ceramics, J. Am. Ceram. Soc. 96 (2013) 496-502.

[6] W. Wang, L.D. Wang, W.L. Li, D. Xu, Y.F. Hou, W.P. Cao, Y. Feng and W.D. Fei, Piezoelectric properties of $BaTiO_3$-$CaTiO_3$-$BaZrO_3$ ceramics with compositions near the morphotropic phase boundary, Ceram. Int. 40 (2014) 14907-14912.

[7] Y. Zhang, J. Glaum, C. Groh, M.C. Ehmke, J.E. Blendell, K.J. Bowman and M.J. Hoffman, Correlation between piezoelectric properties and phase coexistence in $(Ba,Ca)(Ti,Zr)O_3$ ceramics, J. Am. Ceram. Soc. 97 (2014) 2885-2891.

[8] F. Benabdallah, C. Elissalde, U.C.C. Seu, D. Michau, A.P.-Quintin, M. Gayot, P. Garreta, H. Khemakhem and M. Maglione, Structure–microstructure–property relationships in lead-free BCTZ piezoceramics processed by conventional sintering and spark plasma sintering, J. Eur. Ceram. Soc. 35 (2015) 4153-4161.

[9] Y. Bai, A. Matousek, P. Tofel, V. Bijalwan, B. Nan, H. Hughes and T.W. Button, $(Ba,Ca)(Zr,Ti)O_3$ lead-free piezoelectric ceramics-The critical role of processing on properties, J. Eur. Ceram. Soc. 35 (2015) 3445-3456.

[10] V.S. Puli, A. Kumar, D.B. Chrisey, M. Tomozawa, J.F. Scott, R.S. Katiyar, Barium zirconate-titanate/barium calcium-titanate ceramics via sol-gel process: novel high-energy-density capacitors, J. Phys D: Appl. Phys. 44 (2011) 395403-1-10.

[11] Z. Wang, K. Zhao, X. Guo, W. Sun, H. Jiang and X. Han, et al., Crystallization, phase evolution and ferroelectric properties of sol–gel-synthesized $Ba(Ti_{0.8}Zr_{0.2})O_3$-x$(Ba_{0.7}Ca_{0.3})TiO_3$ thin films, J. Mater. Chem. C 1 (2013) 522-530.

[12] A.R.-Montero, L. Pardo, R.L.-Juárez, A.M. González, M.P. Cruz and M.E.V.-Castrejón, Lead-free $Ba_{0.9}Ca_{0.1}Ti_{0.9}Zr_{0.1}O_3$ piezoelectric ceramics processed below 1300 °C, J. Alloy. Comp. 584 (2014) 28-33.

[13] J.P. Praveen, T. Karthik, A.R. James, E. Chandrakala, S. Asthana and D. Das, Effect of poling process on piezoelectric properties of sol–gel derived BZT-BCT ceramics, J. Eur. Ceram. Soc. 35 (2015) 1785-1798.

[14] K. Castkova, K. Maca, J. Cihlar, H. Hughes, A. Matousek, P. Tofel, Y. Bai and T.W. Button, Chemical synthesis, sintering and piezoelectric properties of $Ba_{0.85}Ca_{0.15}Zr_{0.1}Ti_{0.9}O_3$ Lead-Free ceramics, J. Am. Ceram. Soc. 98 (2015) 2373-2380.

[15] Z. Wang, J. Wang, X. Chao, L. Wei, B. Yang, D. Wang and Z. Yang, Synthesis, structure, dielectric, piezoelectric, and energy storage performance of $(Ba_{0.85}Ca_{0.15})(Ti_{0.9}Zr_{0.1})O_3$ ceramics prepared by different methods, J. Mater. Sci.: Mater. Electron. 27 (2016) 5047-5058.

[16] Z. Sun, Y. Pu, Z. Dong, Y. Hu, P. Wang, X. Liu and Z. Wang, Impact of fast microwave sintering on the grain growth, dielectric relaxation and piezoelectric properties on $Ba_{0.18}Ca_{0.02}Ti_{0.09}Zr_{0.10}O_3$ lead-free ceramics prepared by different methods, Mater. Sc. Eng. B 185 (2014) 114-122.

[17] W.R. Buessem, L.E. Cross and A.K. Goswami, Phenomenological theory of high permittivity in fine-grained barium titanate, J. Am. Ceram. Soc., 49 (1966) 33-36; Effect of two-dimensional pressure on the permittivity of fine- and coarse-grained barium titanate, J. Am. Ceram. Soc. 49 (1966) 36-39.

[18] H.T. Martirena and J.C. Burfoot, Grain-size effects on properties of some ferroelectric ceramics, J. Phys. C Solid State Phys. 7 (1974) 3182-3192.

[19] C.A. Randall, N. Kim, J.-P. Kucera, W. Cao and T.R. Shrout, Intrinsic and Extrinsic Size Effects in Fine-Grained Morphotropic-Phase-Boundary Lead Zirconate Titanate Ceramics, J. Am. Ceram. Soc. 81 (1998) 677-688.

[20] T.M. Shaw, S. Trolier-McKinstry and P.C. McIntyre, The Properties of Ferroelectric Thin Films at Small Dimensions, Annu. Rev. Mater. Sci. 30 (2000) 263-298.

[21] M. A. Rafiq, M. E. Costa, and P. M. Vilarinho, ACS Appl. Mater. Interfaces, **8** (2016), 33755-33764.

[22] A.C. Larson, R.B. Von Dreele, GSAS. Report LAUR, Los Alamos National Laboratory Report LAUR 86 (2004) 748.

[23] B.H. Toby, EXPGUI, a graphical user interface for GSAS, J. Appl. Crystallogr. 34 (2001) 210-213.

[24] K. Momma and F. Izumi, VESTA 3 for three-dimensional visualization of crystal, volumetric and morphology data, J. Appl. Crystallogr. 44 (2011) 1272-1276.

[25] D.S. Keeble, F. Benabdallah, P.A. Thomas, M. Maglione, and J. Kreisel, Revised structural phase diagram of $(Ba_{0.7}Ca_{0.3}TiO_3)$-$(BaZr_{0.2}Ti_{0.8}O_3)$, Appl. Phys. Lett. 102 (2013) 092903-1-5.

[26] J. Gao, L. Zhang, D. Xue, T. Kimoto, M. Song, L. Zhong, and X. Ren, Symmetry determination on Pb-free piezoceramic $0.5Ba(Zr_{0.2}Ti_{0.8})O_3$-$0.5(Ba_{0.7}Ca_{0.3})TiO_3$ using convergent beam electron diffraction method, J. Appl. Phys. 115(5) (2014) 054108-1-5.

[27] A.B. Haugen, J.S. Forrester, D. Damjanovic, B. Li, K.J. Bowman and J.L. Jones, Structure and phase transitions in $0.5(Ba_{0.7}Ca_{0.3}TiO_3)$-$0.5(BaZr_{0.2}Ti_{0.8}O_3)$ from $-100\,°C$ to $150\,°C$, J. Appl. Phys. 113 (2013) 014103-1-5.

[28] W. Li, Z. Xu, R. Chu, P. Fu and G. Zang, Polymorphic phase transition and piezoelectric properties of $(Ba_{1-x}Ca_x)(Ti_{0.9}Zr_{0.1})O_3$ lead-free ceramics, Physica B 405 (2010) 4513-4516.

[29] D. Damjanovic, A. Biancoli, L. Batooli, A. Vahabzadeh, and J. Trodahl, Elastic, dielectric, and piezoelectric anomalies and Raman spectroscopy of $0.5Ba(Ti_{0.8}Zr_{0.2})O_3$-$0.5(Ba_{0.7}Ca_{0.3})TiO_3$, Appl. Phys. Letts., 100 (2012) 192907-1-4.

[30] E. V. Ramana, F. Figueiras, A. Mahajan, D. M. Tobaldi, B. F. O. Costa, M. P. F. Graça and M. A. Valente, Effect of Fe-doping on the structure and magnetoelectric properties of $(Ba_{0.85}Ca_{0.15})(Ti_{0.9}Zr_{0.1})O_3$ synthesized by a chemical route, J. Mater. Chem. C, 4 (2016) 1066-1079.

[31] Y. Tian, X. Chao, L. Jin, L. Wei, P. Liang and Z. Yang, Polymorphic structure evolution and large piezoelectric response of lead-free $(Ba,Ca)(Zr,Ti)O_3$ ceramics, Appl. Phys. Lett. 104 (2014) 112901-1-5.

[32] D. Damjanovic, A morphotropic phase boundary system based on polarization rotation and polarization extension, Appl. Phys. Lett. 97 (2010) 062906-1-3.

[33] M. E. Lines and A. M. Glass, Principles and applications of ferroelectrics and related materials; Clarendon Press: Oxford, 1979.

[34] G. Arlt, D. Hennings and G.de With, Dielectric properties of fine☐grained barium titanate ceramics, J. Appl. Phys. 58 (1985) 1619-1625.

[35] M. P. McNeal, S.-J. Jang and R. E. Newnham, The effect of grain and particle size on the microwave properties of barium titanate ($BaTiO_3$), J. Appl. Phys. 83 (1998) 3288-3297.

[36] D. Hennings, A. Schnell and G. Simon, Diffuse ferroelectric phase transitions in $Ba(Ti_{1-y}Zr_y)O_3$ ceramics, J. Am. Ceram. Soc. 65 (1982) 539-544.

[37] K. Uchino and S. Nomura, Critical exponents of the dielectric constants in diffused-phase-transition crystals, Ferroelectrics 44 (1982) 55-61.

[38] X. Tang and H.L. Chan, Effect of grain size on the electrical properties of (Ba,Ca)(Zr,Ti)$O_3$(Ba,Ca)(Zr,Ti)$O_3$ relaxor ferroelectric ceramics, J. Appl. Phys. 97 (2005) 034109-1-6.

[39] Y. Tian, X. Chao, L. Wei, P. Liang, and Z. Yang, Phase transition behavior and electrical properties of lead-free $(Ba_{1-x}Ca_x)(Zr_{0.1}Ti_{0.9})O_3$ piezoelectric ceramics, J. Appl. Phys. 113 (2013) 184107-1-7.

[40] J. Hao, W. Bai, W. Li and J. Zhai, Correlation between the microstructure and electrical properties in high-performance $(Ba_{0.85}Ca_{0.15})(Zr_{0.1}Ti_{0.9})O_3$ lead-free piezoelectric ceramics, J. Am. Ceram. Soc. 95 (2012) 1998-2006.

[41] H. Amorín, R. Jiménez, M. Deluca, J. Ricote, T. Hungría, A. Castro and M. Algueró, Nanostructuring effects in piezoelectric BiSc$O_3$–PbTi$O_3$ Ceramics, J. Am. Ceram. Soc. 97 (2014) 2802-2809.

[42] Q. Tan and D. Viehland, Grain size dependence of relaxor characteristics in La-modified lead zirconate titanate, Ferroelectrics 193 (1997) 157-165.

[43] Z. Zhao, V. Buscaglia, M. Viviani, M.T. Buscaglia, L. Mitoseriu, A. Testino, M. Nygren, M. Johnsson and P. Nanni, Grain-size effects on the ferroelectric behavior of dense nanocrystalline BaTi$O_3$ ceramics, Phys. Rev. B  70 (2004) 024107-1-8.

[44] A.V. Polotai, A.V. Ragulya and C.A. Randall, Preparation and size effect in pure nanocrystalline barium titanate ceramics, Ferroelectrics 288 (2003) 93-102.

[45] P. Bharathi and K.B.R. Varma, Grain and the concomitant ferroelectric domain size dependent physical properties of $Ba_{0.85}Ca_{0.15}Zr_{0.1}Ti_{0.9}O_3$ ceramics fabricated using powders derived from oxalate precursor route, J. Appl. Phys. 116 (2014) 164107.

[46] L. Zhang, W. L. Zhong, Y.G. Wang and P.L. Zhang, The cell volume effect in barium strontium titanate, Solid State Commun. 104 (1997) 263-266.

[47] W.J. Merz, The effect of hydrostatic pressure on the Curie point of barium titanate single crystals, Phys. Rev. 78 (1950) 52-54.

[48] G.A. Samara, Pressure and Temperature Dependences of the Dielectric Properties of the Perovskites $BaTiO_3$ and $SrTiO_3$, Phys. Rev. 151 (1966) 378-386.

[49] T. Qi, I. Grinberg and A.M. Rappe, Correlations between tetragonality, polarization, and ionic displacement in $PbTiO_3$-derived ferroelectric perovskite solid solutions, Phys. Rev. B 82 (2010) 134113-1-5.

[50] R.E. Eitel, S.J. Zhang, T.R. Shrout, C.A. Randall and I. Levin, Phase Diagram of the Perovskite System, J. Appl. Phys. 96 (2004) 2828-2831.

[51] C.A. Randall, R. Eitel, B. Jones, T.R. Shrout, D.I. Woodward and I.M. Reaney, Investigation of a high Tc piezoelectric system: $(1-x)Bi(Mg_{1/2}Ti_{1/2})O_3-(x)PbTiO_3$, J. Appl. Phys. 95 (2004) 3633-3639.

[52] R. Herbiet, U. Robels, H. Dederichs and G. Arlt, Domain wall and volume contributions to material properties of PZT ceramics, Direct evaluation of domain⬚wall and intrinsic contributions to the dielectric and piezoelectric response and their temperature dependence on lead zirconate⬚titanate ceramics, Ferroelectrics 98 (1989) 107-121.

[53] Q.M. Zhang, H. Wang, N. Kim and L.E. Cross, Direct evaluation of domain⬚wall and intrinsic contributions to the dielectric and piezoelectric response and their temperature dependence on lead zirconate⬚titanate ceramics, J. Appl. Phys., 75 (1994) 454-459.

[54] R. Herbeit, U. Robels, H. Dederichs and G. Arlt, Domain wall and volume contributions to material properties of PZT ceramics, Ferroelectrics 98 (1989) 107-121.

[55] E.I. Bondarenko, V.Y. Topolov and A.V. Turik, The role of 90° domain wall displacements in forming physical properties of perovskite ferroelectric ceramics, Ferroelectr. Lett. 13 (1991) 13-19.

[56] H. Orihara, S. Hashimoto and Y. Ishibashi, A Theory of D-E Hysteresis Loop Based on the Avrami Model, J. Phys. Soc. Jpn. 63 (1994) 1031-1035.

[57] G. Arlt and N.A. Pertsev, Force constant and effective mass of 90° domain walls in ferroelectric ceramics, J. Appl. Phys. 70 (1991) 2283-2289.

[58] H. Amorín, R. Jiménez, J. Ricote, A. Castro and M. Algueró, Nanoscale Ferroelectrics and Multiferroics: Key Processing and Characterization Issues, and Nanoscale Effects , John Wiley & Sons, Ltd. 2016, pp 512-553.

[59] A.F. Devonshire, Theory of barium titanate, Philos. Mag. 40 (1949) 1040-1063.

[60] M.J. Haun, E. Furman, S.J. Jang and L.E. Cross, Thermodynamic theory of the lead zirconate-titanate solid solution system, part I: Phenomenology, Ferroelectrics 99 (1989) 13-25.

[61] V.V. Shvartsman and A.L. Kholkin, Investigation of the ferroelectric-relaxor transition in $PbMg_{1/3}Nb_{2/3}O_3$–$PbTiO_3$ ceramics by piezoresponse force microscopy, J. Appl. Phys. 108 (2010) 42007-1-6.

[62] K.-H. Yang, N.-J. Ho, H.-Y. Lu, Deformation Microstructure in (001) Single Crystal Strontium Titanate by Vickers Indentation, J. Am. Ceram. Soc. 92 (2009) 2345-2353.

[63] W.C. Oliver, G.M. Pharr, An improved technique for determining hardness and elastic modulus using load and displacement sensing indentation experiments, J. Mater. Res. 7 (1992) 1564-1583.

[64] T. Ogawa, K. Ishii, T. Matsumoto and T. Nishina, Poling Field Dependence of Longitudinal and Transverse Wave Velocities, Young's Modulus, and Poisson's Ratio in Piezoelectric Ceramics, Jpn. J. Appl. Phys. Part 2, 51 (2012) 09LD03-1-12.

[65] T.Van Dijk and A.J. Burggraaf, Grain boundary effects on ionic conductivity in ceramic $Gd_xZr_{1-x}O_{2-(x/2)}$ solid solutions, Phys. Status Solidi (a) 63 (1981) 229-240.

[66] M.J. Verkerk, B.J. Middelhuis and A.J. Burggraaf, Effect of grain boundaries on the conductivity of high-purity $ZrO_2$-$Y_2O_3$ ceramics, Solid State Ionics 6 (1982) 159.

[67] J. Fleig and J. Maier, The impedance of ceramics with highly resistive grain boundaries: validity and limits of the brick layer model, J. Euro. Ceram. Soc., 19 (1999) 693-696.

[68] J.C.C. Abrantes, J.A. Labrincha, J.R. Frade, Applicability of the brick layer model to describe the grain boundary properties of strontium titanate ceramics, J. Euro. Ceram. Soc., 20 (2000) 1603-1609.

[69] S.H. Yoon, C.A. Randall and K.H. Hur, Effect of acceptor concentration on the bulk electrical conduction in acceptor (Mg)-doped $BaTiO_3$, J. Appl. Phys. 107 (2010) 103721-1-8.

[70] R. Waser, T. Baiatu and K.H. Härdtl, dc Electrical Degradation of Perovskite-Type Titanates: I, Ceramics, J. Am. Ceram. Soc. 73 (1990) 1645-1653; dc Electrical Degradation of Perovskite-Type Titanates: II, Single Crystals, J. Am. Ceram. Soc. 73 (1990) 1654-1662.

[71] G.M. Choi, H.L. Tuller and D. Goldschmidt, Electronic-transport behavior in single-crystalline $Ba_{0.03}Sr_{0.97}TiO_3$, Phys. Rev. B 34 (1986) 6972-6979.

[72] H. Neumann and G. Arlt, Maxwell-Wagner relaxation and degradation of $SrTiO_3$ and $BaTiO_3$ ceramics, Ferroelectrics 69 (1986) 179-186.

[73] R. Waser and R. Hagenbeck, Grain boundaries in dielectric and mixed-conducting ceramics, Acta Mater. 48 (2000) 797-825.

[74] G.V. Lewis, C.R.A. Catlow and R.E.W. Casselton, PTCR Effect in $BaTiO_3$, J. Am. Ceram. Soc. 68 (1985) 555-558.

[75] M. Demartin and D. Damjanovic, Dependence of the direct piezoelectric effect in coarse and fine grain barium titanate ceramics on dynamic and static pressure, Appl. Phys. Lett., 68 (1996) 3046-3048.